Flow produced by a free-moving floating magnet driven electromagnetically

Saúl Piedra,[1,*] Joel Román,[2] Aldo Figueroa,[3,†] and Sergio Cuevas[2]
[1]*Centro de Investigación en Ciencias, Universidad Autónoma del Estado de Morelos, Cuernavaca, Morelos 62209, México*
[2]*Instituto de Energías Renovables, Universidad Nacional Autónoma de México, Privada Xochicalco s/n Temixco, Morelos 62580, México*
[3]*CONACYT - Centro de Investigación en Ciencias, Universidad Autónoma del Estado de Morelos, Cuernavaca, Morelos 62209, México*

(Received 8 May 2017; published 30 April 2018)

The flow generated by a free-moving magnet floating in a thin electrolyte layer is studied experimentally and numerically. The magnet is dragged by a traveling vortex dipole produced by a Lorentz force created when a uniform dc current injected in the electrolyte interacts with the magnetic field of the same magnet. The problem represents a typical case of fluid-solid interaction but with a localized electromagnetic force promoting the motion. Classical wake flow structures are observed when the applied current varies in the range of 0.2 to 10 A. Velocity fields at the surface of the electrolyte are obtained for different flow conditions through particle image velocimetry. Quasi-two-dimensional numerical simulations, based on the immersed boundary technique that incorporates the fluid-solid interaction, reproduce satisfactorily the dynamics observed in the experiments.

DOI: 10.1103/PhysRevFluids.3.043702

I. INTRODUCTION

The flow produced by the motion of a solid body in a viscous fluid is a classical problem relevant in many contexts, such as animal locomotion and man-made devices. When a solid body moves in a viscous fluid, a vortical wake develops whose characteristics depends on the shape of the body and the flow intensity. In this situation, the presence of instabilities and the appearance of periodic arrays of vortices is a common feature. Afanasyev [1] clearly distinguishes between towed objects and self-propelled bodies. In the first case, the object exerts a force on the fluid equal to the drag force experienced by the object and acting in the opposite direction so that a continuous transfer of momentum to the fluid is present. When a self-propelled body moves with a constant speed, thrust must be equal to the drag force and of opposite direction, therefore a zero-momentum flow is generated.

With the aim of describing the wakes and vortex streets created by moving objects, Afanasyev and Korabel [2] used spatially localized electromagnetic forces acting on the fluid as a virtual body. The use of electromagnetic forcing in conducting fluids provides a nonintrusive mechanism to generate vortical flows without the presence of solid objects. In the context of moving objects, this approach offers a reasonable description of far-field flows, that is, flows that are sufficiently far from the object so that the details of the shape of the body are not relevant. To carry out the experimental study, Afanasyev and Korabel injected a uniform dc current in a thin layer of electrolyte while a

*Current address: CONACYT-CIDESI, Centro Nacional de Tecnologías Aeronáuticas (CENTA), Colón, Queretaro De Arteaga, México.
†Corresponding author: alfil@uaem.mx

permanent magnet was dragged above the fluid, producing a Lorentz force that stirred the liquid. A similar procedure was recently implemented to study different vortex patterns and wake transitions in electrolytes [3]. Vortical wakes are also observed when a magnet is dragged underneath a liquid metal layer although injected currents are not required since, owing to the high electric conductivity of the fluid, induced currents are strong enough to generate significant Lorentz forces [4,5]. A localized Lorentz force created by the interaction of a confined magnetic field with either applied or induced currents is referred to as a magnetic obstacle since it is able to produce vortex patterns that, in some aspects, resemble those observed in flows past solid obstacles [6,7].

It is well known that the application of a localized force to a volume of viscous fluid generates a vortex dipole [8,9]. If the force is impulsive, a translating vortex dipole appears. A vortex dipole is easily created in a thin electrolyte layer when a uniform electric current interacts with the field of a small magnet located underneath the layer. In this case, the localized Lorentz force acts as a source of momentum, creating a jet in the zone of highest magnetic field intensity that eventually is spread to form a pair of counter-rotating vortices [9,10]. An entirely new situation arises when the magnet is floating freely at the surface of the fluid layer. Under these conditions, the magnet is driven by the vortex dipole generated by the interaction of the uniform electric current and its own magnetic field. Therefore, the magnet acts as a surfing obstacle driven by the flow produced by the electromagnetic interaction, the dynamics of its motion being dictated by the hydrodynamic forces acting upon it. Evidently, the magnet experiences a drag force that is always in the direction opposite to its motion. The previously described situation is precisely the one analyzed in this work, where an experimental and numerical study was carried out to explore the dynamics of the flow generated by a surfing magnet. To the best of our knowledge, this is the first reported study of the flow produced by a free-moving floating magnet in an electrolyte layer.

The paper is organized as follows. In Sec. II, the experimental setup is described. In Sec. III, the mathematical quasi-two-dimensional model is formulated, based on the solution of the conservation equations and the immersed boundary technique that considers the solid-fluid interactions. In Sec. IV, the experimental observations are shown and different flow structures formed in the wake of the magnet are presented. In addition, numerical results are compared with experimental observations, and simulations are used to explore other characteristics of the flow. Finally, in Sec. V, some concluding remarks are offered.

II. EXPERIMENTAL SETUP

The experimental device consists of a rectangular container 100 cm long, 47 cm wide, and 5 cm high. The sides of the container are made of Plexiglas and the bottom is made of glass (see Fig. 1). The container is partially filled with an electrolytic solution of potassium chloride (KCl) at 20% by weight with a layer thickness of 0.5 cm, so that the total volume of liquid is 1900 cm^3. The mass density, kinematic viscosity, and electrical conductivity of the electrolyte are $\rho = 1.09 \times 10^3$ Kg/m^3, $\nu = 10^{-6}$ m^2/s, and $\sigma = 30.9$ S/m, respectively. Two electrodes (square graphite rods of 1 cm $\times$ 1 cm cross section and 80 cm in length) were placed along the two long sides of the container and connected to a power supply that allowed us to inject a uniform dc current that varied from 200 mA to 10 A. The electrodes were located inside chambers (bubble traps) that allow the electric current to flow while preventing the bubbles from electrolysis from invading the main flow region. A neodynium-iron-boron cylindrical dipole magnet of 4 mm in diameter and maximum magnetic field strength of 0.165 T was kept afloat at the surface of the electrolyte layer by sticking it to a circular plastic film of 6.3 mm in diameter. The interaction of the electric current with the localized magnetic field generates the Lorentz force that promotes the vortex dipole that drives the magnet. The flow was visualized using vegetable ink poured at the surface. The trajectory of the magnet was recorded at 24 fps with a high-definition Nikon D84 with resolution of 1920 $\times$ 1080 pixels, while an image analysis algorithm was used to detect the pixels that correspond to the boundary of the solid. The algorithm determines the time evolution of the solid motion and locates the centroid in all frames. The velocity of the magnet as a function of time can be computed using the trajectory of its

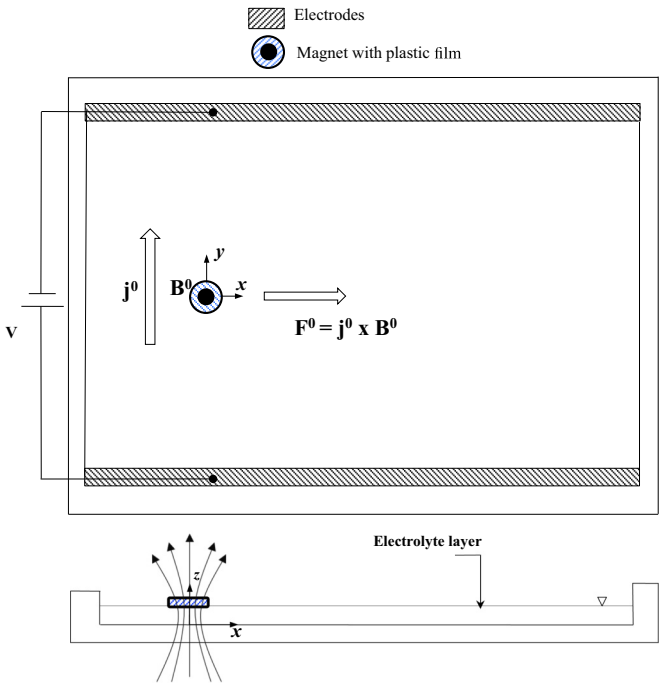

FIG. 1. Sketch of the experimental device, not drawn to scale. Upper panel: plan view. Lower panel: lateral view. The magnetic field $\mathbf{B}^0$ is generated by a permanent magnet floating on the surface of the fluid layer. The electrical current $\mathbf{j}^0$ is injected through two cooper electrodes. The main direction of the Lorentz force is denoted by $\mathbf{F}^0$.

centroid. Since the weight of the magnet is 0.1 g and depresses the surface 0.3 mm (approximately 5% of the fluid layer thickness), the surface deformation has a negligible effect on the flow dynamics. In order to avoid the transient, all observations were made 40 cm far from the initial position of the magnet. The measurements of the velocity field were obtained by a particle image velocimetry (PIV) system. Spherical glass particles (10 μm diameter) were seeded in the free surface of the electrolyte layer and illuminated using LEDs. The recorded images were analyzed using the software PIVLAB [11].

III. MATHEMATICAL MODEL

Mathematical and numerical formulations were implemented to simulate the system described in Sec. II. The mathematical model is based on the immersed boundary method which was originally developed by Peskin [12]. This method allows us to incorporate internal geometries using a simple rectangular fixed grid. The use of this formulation avoids the generation of a complex grid that has to conform to the surface of the internal boundary. In this particular case, in the two-dimensional approximation, it can be assumed that the magnet attached to the circular plastic film immersed in the electrolyte solution constitutes a solid internal boundary. Then, using a regular Cartesian grid to discretize the whole domain, some control volumes will be included in the fluid region and others in the solid region. One of the main goals of the immersed boundary method is to identify the cells inside and outside the solid; for this purpose, we define an indicator field using the Heaviside step function as follows [13]:

$$I(\mathbf{x}) = \begin{cases} 1 & \text{inside the fluid,} \\ 0 & \text{inside the solid.} \end{cases} \tag{1}$$

The indicator function [Eq. (1)] assigns a different constant value to each phase, and it is constructed using the facts that the interface marks the jump in the indicator function and that this jump becomes a steep gradient on the Cartesian grid. The indicator field is updated at each time step using the same strategy reported in [14]. Once the indicator field is calculated, the velocity in any cell of the computational domain is given by

$$\mathbf{u}(\mathbf{x}) = I(\mathbf{x})\mathbf{u}_f(\mathbf{x}) + [1 - I(\mathbf{x})]\mathbf{u}_s(\mathbf{x}), \tag{2}$$

where subindexes f and s denote the fluid and solid regions, respectively. The velocities in the fluid and the solid regions must be computed in order to generate the velocity field in the whole domain. From the mathematical point of view, since the indicator field is represented as a Heaviside function, a no-slip boundary condition at the solid surface is imposed. However, the numerical implementation of the discrete form of the step function creates a transition zone where the indicator function takes values from zero inside the solid to one outside of it. Hence, in a strict sense, the imposition of the no-slip boundary condition at the interface depends on the shape and thickness of such transition zone. This is a well-known behavior of the immersed boundary and fictitious domain methods, and many approximations have been developed to improve the accuracy of the solutions, reducing the effect of the transition zone; some examples can be found in [13]. Several formulations of the immersed boundary method have been developed in recent years in order to simulate freely moving bodies in a viscous fluid; for instance see [15,16]. The main idea is to mark the cells of the grid where the solid is localized and solve the Navier-Stokes equations coupled with the equations of motion of a rigid body, to compute the linear and angular velocities of the body and calculate its new position in the fluid domain at every time step. In this investigation, we followed the formulation given by [17,18] in which in the first step the solid cells are solved as a fluid, as in the fictitious domain method; however, in order to emulate the rigid behavior of the solid, it is approximated as a fictitious fluid with a relatively high viscosity. Using this approach it is possible to solve the following mass and momentum equations for the whole domain with variable density and viscosity:

$$\nabla \cdot \mathbf{u} = 0, \tag{3}$$

$$\frac{\partial \rho \mathbf{u}}{\partial t} + \nabla \cdot \rho \mathbf{u}\mathbf{u} = -\nabla p + \nabla \cdot \mu(\nabla \mathbf{u} + \nabla^T \mathbf{u}) + I(\mathbf{j}^0 \times \mathbf{B}^0), \tag{4}$$

where p is the pressure, $\mathbf{B}^0$ is the magnetic field produced by the permanent magnet, $\mathbf{j}^0$ is the applied current density, ρ is the mass density, and μ is the dynamic viscosity. The Lorentz force term in the momentum equations is multiplied by the indicator function since it is only applied on the fluid. Due to the size of the permanent magnet, the normal component of the magnetic field $B_z^0(x, y)$ was modeled by a Gaussian distribution that approximates very well the distribution of a small magnetic dipole [19,20]. The velocity computed from the momentum equations does not necessarily satisfy the rigidity condition in the solid region, therefore the velocity field calculated by the flow solver is averaged over the solid domain to obtain the velocity of the centroid of the body and the angular velocity as follows:

$$M_s \mathbf{u}_{\mathrm{sc}}^{n+1} = \int (1 - I)\rho_s \mathbf{u}\, dV, \tag{5}$$

$$\mathbf{I}_s \Omega_z^{n+1} = \int (1 - I)\mathbf{r} \times \rho_s \mathbf{u}\, dV, \tag{6}$$

where M_s is the mass of the solid, $\mathbf{u}_{\mathrm{sc}}$ is the velocity of the centroid of the solid, $\mathbf{I}_s$ is the moment of inertia tensor, and Ω_z is the angular velocity of the solid body. Once the translational and angular velocities of the body are computed, the corrected velocity field in the solid region ($\mathbf{u}_s$) is obtained:

$$\mathbf{u}_s = \mathbf{u}_{\mathrm{sc}} + \mathbf{r} \times \Omega_z \hat{k}, \tag{7}$$

where $\mathbf{r}$ is the position vector, that is, the distance to any point inside the solid from the center of rotation of the rigid body. Since the solid is moving through the fluid, the material properties in the Cartesian grid, such as the density and viscosity, depend on the position and time and must be computed at every time step. The determination of these properties is done through the indicator field:

$$\rho(\mathbf{x},t) = \rho_s(1 - I(\mathbf{x},t)) + \rho_f I(\mathbf{x},t), \tag{8}$$

$$\mu(\mathbf{x},t) = \mu_s(1 - I(\mathbf{x},t)) + \mu_f I(\mathbf{x},t). \tag{9}$$

It is convenient to introduce the following dimensionless variables:

$$\mathbf{x}^* = \frac{\mathbf{x}}{d}, \quad \mathbf{u}^* = \frac{\mathbf{u}}{u_o}, \quad \rho^* = \frac{\rho}{\rho_f}, \quad p^* = \frac{p}{\rho_f u_o^2}, \quad \mu^* = \frac{\mu}{\mu_f},$$
$$\mathbf{j}^* = \frac{\mathbf{j}}{j_0}, \quad \mathbf{B}^* = \frac{\mathbf{B}}{B_0}, \quad t^* = \frac{t}{d^2/\nu_f},$$

where d is the diameter of the magnet and $u_o = \nu_f/d$ is the characteristic velocity, whereas the magnitudes of the electric current density and magnetic field are denoted by j_0 and B_0, respectively. Additionally, we use a quasi-two-dimensional approach that involves the averaging of the equations in the z direction, normal to the free surface. Then, the averaged mass and momentum balance equations are expressed in dimensionless form as

$$\nabla \cdot \mathbf{u} = 0, \tag{10}$$

$$\frac{\partial \rho \mathbf{u}}{\partial t} + \nabla \cdot \rho \mathbf{u}\mathbf{u} = -\nabla p + \nabla \cdot \mu(\nabla \mathbf{u} + \nabla^T \mathbf{u}) - \frac{\mathbf{u}}{\tau} + QI(\mathbf{j}^0 \times \mathbf{B}^0), \tag{11}$$

where the superscript * has been omitted. The third term of the right-hand side of Eq. (11) represents the Rayleigh friction, where τ is the characteristic timescale for the damping of vorticity owing to dissipation in the viscous layers. This term appears due to the averaging of the conservation equations in the z direction, and the inverse of τ is given by [10]

$$\tau^{-1} = \frac{\gamma\left(1 - e^{-\gamma\varepsilon^2}\right)}{\frac{1}{\gamma}\left(1 - e^{-\gamma\varepsilon^2}\right) + \frac{\gamma\varepsilon^4}{2}e^{-\gamma\varepsilon^2} - \varepsilon^2}, \tag{12}$$

where $\gamma = 2.05$ was obtained from experimental measurements, as explained in detail in [10]. In turn, $\varepsilon = h/d$, where h is the depth of the electrolyte layer. The flow is governed by the Lorentz force parameter, $Q = U_0/u_0$, that compares two velocity scales: the scale defined from the balance between Lorentz and viscous forces $U_0 = j_o B d^2/\rho_f \nu_f$ (see [10]) and the viscous velocity scale, $u_0 = \nu_f/d$. In addition to the Lorentz force parameter, the other characteristic parameter of the flow is the ratio of solid and fluid densities, ρ_s/ρ_f. This ratio remains constant in our simulations, namely, $\rho_s/\rho_f = 6.4$.

Summarizing the methodology implemented in the numerical algorithm, in the first stage, the indicator field is updated at every time step using the same strategy reported in [14]. Then, the solid is treated as a fictitious fluid with a relatively high viscosity to emulate the behavior of a solid, in order to compute the velocity field inside the solid with the Navier-Stokes equations [Eqs. (10) and (11)]. In a second step, the velocity field inside the solid is averaged to calculate the translational and rotational velocities of the magnet using Eqs. (5) and (6). Then, the rigidity constraint of the solid body is enforced by correcting the velocity field inside the solid using Eq. (7). Finally, the position of the solid is updated to complete the algorithm. The computational domain consists of a rectangle with free-slip boundary conditions at the lateral walls (where the electrodes are located), whereas no-slip conditions were used for the left and right walls. Considering the diameter of the magnet d as the characteristic length, the size of the computational domain is 84×12, discretized in a regular

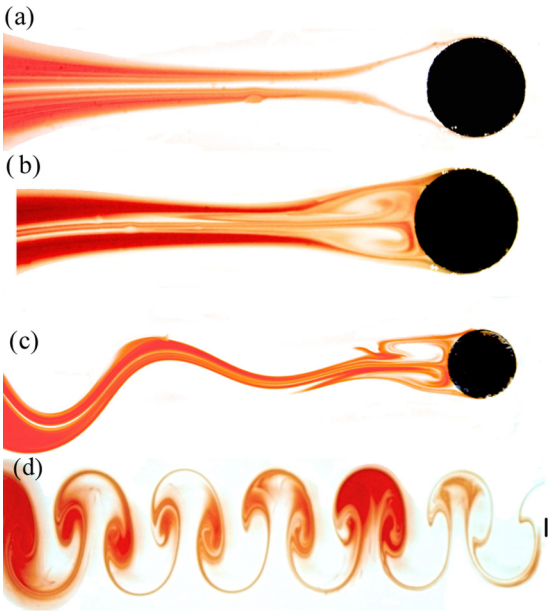

FIG. 2. Experimental visualization of the flow patterns observed for different applied currents. (a) $I =$ 400 mA. (b) $I = 2$ A. (c) and (d) $I = 10$ A. (c) and (d) correspond to the close and far wake regions, respectively. The black disk in (a), (b), and (c) indicates the size of the magnet. The solid line in (d) indicates the diameter of the magnet.

grid of 1792×256 control volumes in the x and y directions, respectively. The time step was fixed at 10^{-5} for all the simulations to give consistent results.

IV. RESULTS

The flow starts when the electric current is injected and interacts with the magnetic field, producing a Lorentz force in the fluid that promotes a traveling vortex dipole with the floating magnet at its center. The jet-like flow produced in the main direction of the Lorentz force (x direction), along the symmetry axis of the vortex dipole, exerts a hydrodynamic force that accelerates the magnet. Therefore, the magnetic source and the vortex dipole travel together. We examined the flow for several applied currents from 200 mA to 10 A. Three different flow structures were found in the experiments, as observed in Fig. 2. For low applied currents ($I < 900$ mA) a steady flow was found where the magnet moves slowly on a straight path [Fig. 2(a)]. When the current is $0.9 < I < 3$ A, a steady wake is observed with two counter-rotating vortices attached behind the moving magnet and aligned in the direction of motion [see Fig. 2(b)]. For high applied currents ($I > 3$ A) the wake becomes unstable and vortex shedding appears behind the magnet. The vortex street formed behind the magnet in the close and far wake regions can be observed in panels (c) and (d) of Fig. 2, respectively, for a current intensity of 10 A. It is important to note that this vortex street is similar to the vón Kármán vortex street that appears in the flow past a fixed cylinder [21].

In order to examine quantitatively the flow, PIV measurements were carried out. The velocity fields for the previous three cases are shown in Fig. 3. PIV measurements were taken far from the initial position of the magnet in order to analyze a well developed flow. Figure 3(a) shows a well defined symmetric vortex dipole that travels with the magnet. When the current is increased to 2 A [see Fig. 3(b)], counter-rotating vortices are elongated in the direction opposite to the magnet motion while the jet aligned with this direction is intensified. Figure 3(c) shows the velocity field for $I = 10$ A where the vortex shedding appears.

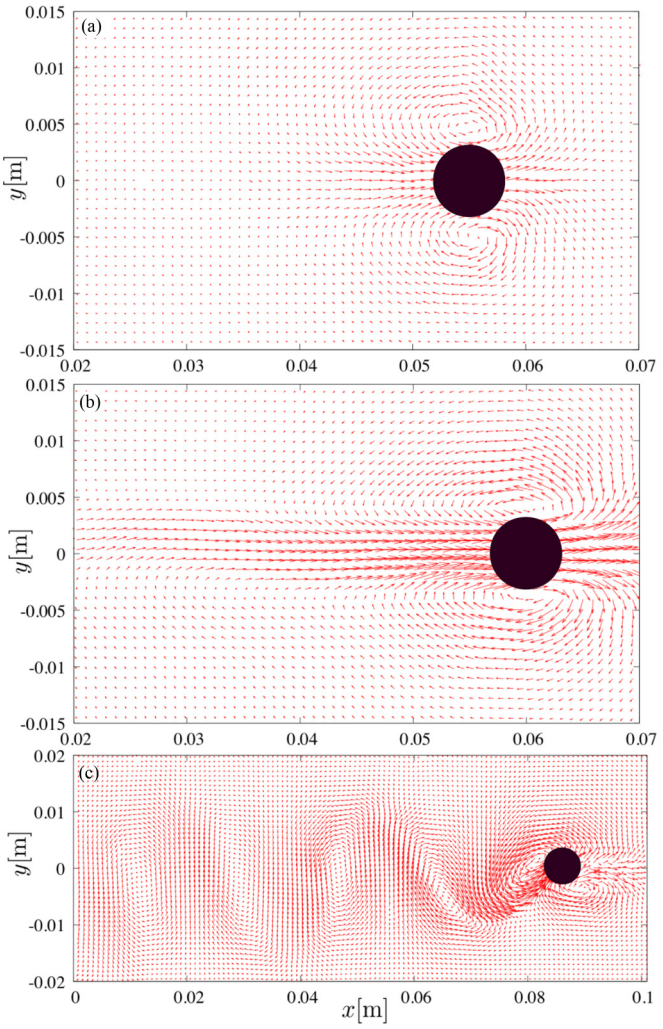

FIG. 3. Velocity fields for three different applied currents. (a) $I = 400$ mA. (b) $I = 2$ A. (c) $I = 10$ A. For the velocity scale see Fig. 5. Experimental measurements.

The tracking of the position of the traveling magnet for $I = 10$ A reveals that it moves in a sinusoidal trajectory, changing its path when a vortex is shed (see Fig. 4). The dimensionless axial position of the magnet x^* is almost a linear function of time, whereas the transversal position y^* exhibits a sinusoidal oscillation in which the amplitude is about 0.4 diameters. The latter implies acceleration of the solid obstacle as it travels. Figure 5 shows the time dependence of the axial, u, and transversal, v, velocity components of the moving magnet for $I = 10$ A. The transversal component of velocity has a large oscillation around zero, with an absolute maximum value about 0.5 cm/s, consistent with the zigzag trajectory of the magnet. The axial motion presents also an oscillating velocity but with a nonzero average velocity given by $u_{\mathrm{av}} = 1.88$ cm/s. Note that the maximum values of the axial velocity occur at instants where the transversal velocity is zero. Similarly to the case of ascending gas bubles [14], it was found that the axial velocity component oscillates with a frequency that is twice the frequency of the transversal velocity. Therefore, the full motion of the magnet is composed of a periodic oscillation with a main horizontal motion with a constant average

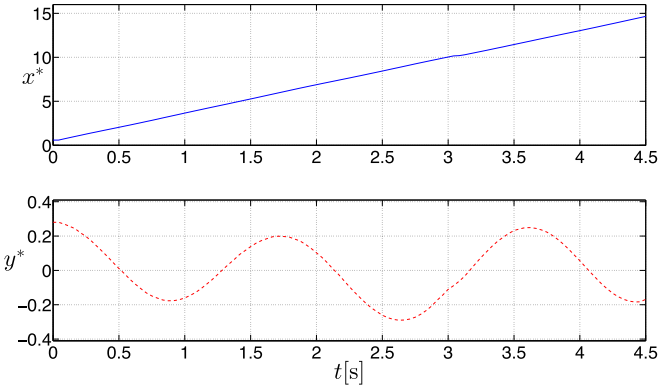

FIG. 4. Position of the moving magnet as a function of time. Upper panel: Horizontal position. Lower panel: Vertical position. $I = 10$ A. Experimental measurements.

velocity. A Reynolds number can be calculated based on the velocity of the magnet. For the case of the injected current of 10 A, $\mathrm{Re} = u_{\mathrm{av}} d/\nu_f = 118.5$.

We performed numerical simulations following the model described in Sec. III. After solving the velocity and pressure fields for the parameters used in the experiments, particle tracking was performed in order to emulate the experimental visualizations presented in Fig. 2. Results of particle tracking are shown in Fig. 6. As can be observed, the flow structures found with the numerical simulations compare satisfactorily with the experimental observations. As the applied current (i.e., the Reynolds number) increases, the transition from the flow pattern where no vortices appear behind the magnet [Fig. 6(a)] to the case where two vortices are observed attached to the moving obstacle [Fig. 6(b)], and finally when vortices are shed periodically [Fig. 6(c)], are clearly reproduced by the numerical simulation.

In Fig. 7, the horizontal and vertical positions of the magnet as a function of time are plotted for an applied current of 10 A. The magnet moves in a straight path and eventually begins to oscillate periodically in the transversal direction. The motion of the magnet in the axial direction coincides with the experimental results. Likewise, the transversal periodic motion with an amplitude of about 0.4 diameters is in quantitative agreement with the experiment.

Figure 8 shows the axial and transversal velocity components as a function of time calculated numerically. The results compare satisfactorily with the experimental observations. Initially, the

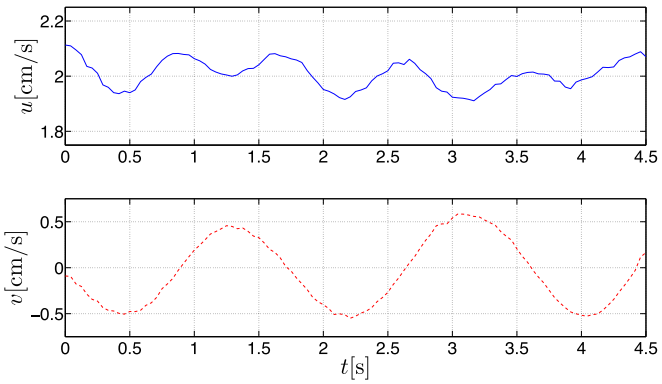

FIG. 5. Time dependence of the axial, u, and transversal, v, velocity components of the moving magnet. $I = 10$ A. Experimental measurements.

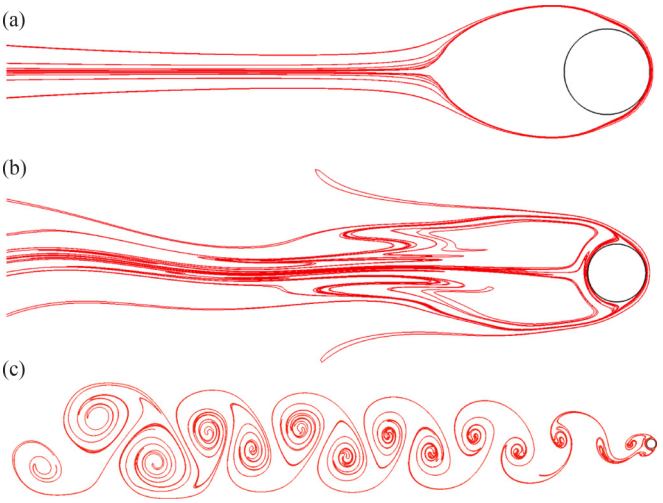

FIG. 6. Flow structure for different applied currents. (a) $I = 400$ mA. (b) $I = 2$ A. (c) $I = 10$ A. Numerical particle tracking visualization.

magnet presents a high acceleration in the axial direction until it reaches a constant average velocity. While at long times the axial component oscillates around a constant average, the transversal component remains initially zero until it starts oscillating periodically, reaching a constant amplitude after a transient time. In agreement with the experimental results, the frequency of the oscillation of velocity in the x direction is twice that of the velocity component in y direction.

The oscillation of the magnet is promoted by a lateral force that appears due to the nonaxisymmetric distribution of the pressure field in the wake behind the magnet. This force, that can be considered as a lift force, pushes the magnet in the y direction, generating a secondary motion in that direction. If the flow is stable and the pressure field in the wake is axisymmetric, the lift force will be zero [see Fig. 6(a)]. However, if the pressure field behind the magnet is nonsymmetric, a lift force over the magnet appears and it will experience a lateral motion [see Fig. 6(c)]. This phenomenon is analogous to the motion of rising bubbles in a Hele-Shaw cell [14,22], in which the buoyancy force push the bubbles to rise vertically but the unstable wake produces a lateral force (lift) that changes the motion of the bubbles to a zigzag path. Therefore, the dynamics of the magnet is governed by two mechanisms.

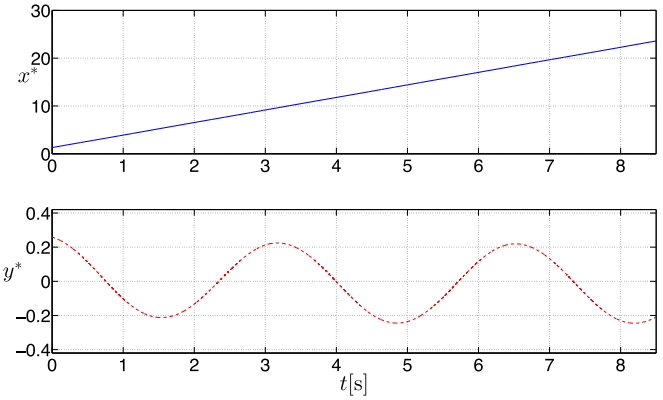

FIG. 7. Position of the moving magnet as a function of time. Upper panel: horizontal position. Lower panel: vertical position. $I = 10$ A. Numerical calculations.

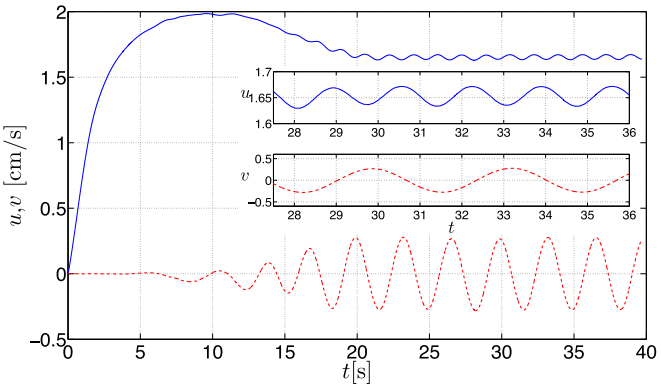

FIG. 8. Time dependence of the horizontal u (continuous line) and vertical v (dashed line) velocity components of the moving magnet. $I = 10$ A. Numerical calculations.

In the first place, the motion in the x direction is promoted by the Lorentz force that creates a jet that drags the magnet. In addition, the transversal motion is generated by a hydrodynamical lift force that appears due to the interaction of the solid with the fluid motion when the magnet's velocity is high enough. As a consequence, the magnet accelerates as it moves in a zigzag manner, that is, the free-moving obstacle suffers changes in its velocity as a function of time.

In Fig. 9, the frequency and amplitude of the motion of the magnet as a function of the Reynolds number based on the average velocity of the magnet, u_{av}, are shown. At low Re, the magnet follows a straight trajectory and thus no oscillation occurs. When the current is increased and the Reynolds number exceeds a threshold (Re $>$ 56), there is a transition zone where the magnet oscillates but it is difficult to determine a dominant frequency and average amplitude. Once this zone is surpassed, the motion of the magnet becomes periodic with a constant amplitude and frequency. Once the vortex shedding appears, frequency and amplitude increase monotonically as a function of the applied current.

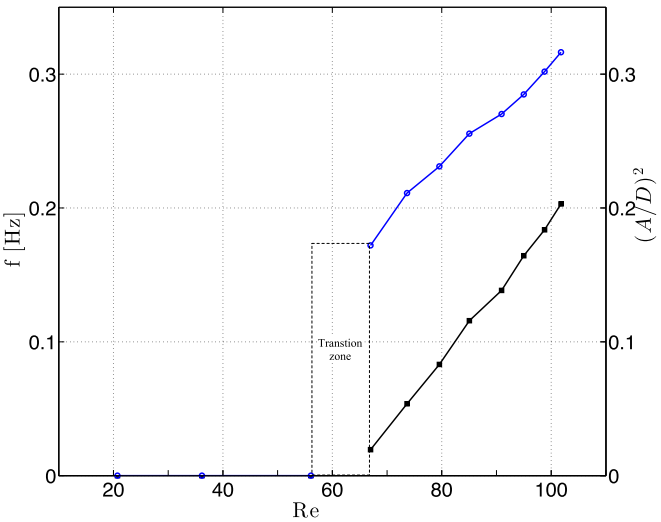

FIG. 9. Frequency (blue curve) and dimensionless amplitude (black curve) of the oscillation of the magnet as function of the Reynolds number, based on the magnet's average velocity u_{av}. Numerical calculations.

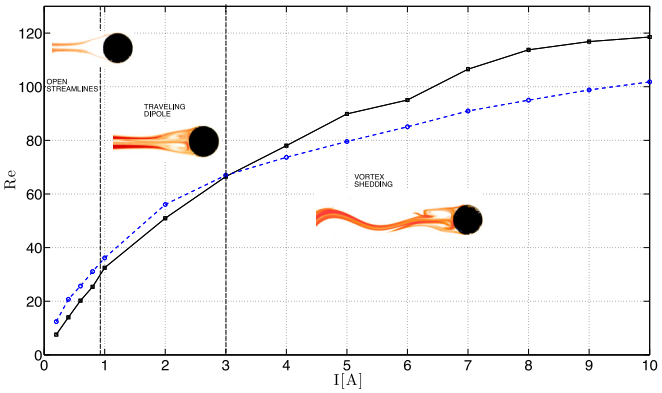

FIG. 10. Map of physical behavior in terms of the Reynolds number and the applied current. The continuous black line and dashed blue line denote the experimental and numerical observations, respectively.

Figure 10 shows a map of physical behavior obtained experimentally and numerically in terms of the Reynolds number and the applied electric current. The zones corresponding to different flow patterns are separated by vertical dashed lines. The Reynolds number is based on the magnet's average velocity and diameter. A reasonable agreement between numerical and experimental results is observed for $I < 3$ A. However, for high applied currents ($I > 3$ A), the model tends to underestimate the velocity. Since at those currents the vortex shedding appears, a possible explanation for the underestimation of the numerical results may be the three-dimensional effects in the wake behind the magnet. Such effects are obviously not taken into account in our quasi-two-dimensional model. However, as we have shown, the main features of the phenomenon are captured by the numerical simulations.

Finally, in order to contrast the difference between the electromagnetically driven free moving obstacle and the uniform flow around a fixed cylinder, numerical simulations were also performed for the latter. The numerical scheme is the same but eliminates the electromagnetic forces and establishes a plug flow from the right to the left in the computational domain. Figure 11 shows that, although vortex streets seem to be qualitatively similar, the frequency and the width of the wake behind the free-moving magnet are lower and larger, respectively, than the fixed solid obstacle wake.

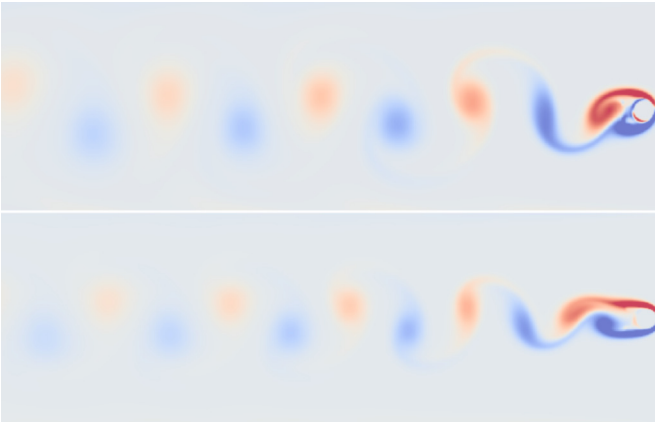

FIG. 11. Vorticity distribution in the wake of an electromagnetically driven free moving obstacle (upper panel) and a fixed solid obstacle (lower panel). Re = 104. Numerical calculations.

V. CONCLUDING REMARKS

The flow generated by a free-moving permanent magnet in a thin electrolyte layer was studied experimentally and theoretically. The Lorentz force promotes the motion of the magnet in the same direction as the jet generated by the traveling vortex dipole. It was possible to identify three different flow structures as function of the applied current. For low currents ($I < 1$ A), a straight motion with open streamlines was observed around the magnet. For larger currents ($1 < I < 3$ A), a vortex dipole develops behind the magnet. Such a vortex dipole becomes unstable for higher currents ($I > 3$ A) and vortex shedding appears in the wake of the magnet. The vortex street seems to be qualitatively similar to the wake behind a fixed solid obstacle; however, the frequency of the vortex shedding behind the magnet is lower and the width of the wake is larger than the fixed solid obstacle wake. Also, it is important to mention that two different interactions between the solid and the fluid are involved in our case of study. The solid is dragged by the vortex dipole generated by the Lorentz force and it accelerates in the same direction as the force. When the motion of the solid is sufficiently fast, the pressure distribution around the magnet becomes nonaxisymmetric, generating a hydrodynamic force perpendicular to the Lorentz force. This lateral force promotes the secondary (zigzag) motion of the magnet. The periodicity of the motion of the solid is dictated by the frequency of the vortex shedding. Each time that a vortex is detached from the body, the solid changes its direction. Thus the flow cannot be described by changing to the frame of reference located on the moving magnet, as can be done when a bluff body moves uniformly in a fluid at rest. The numerical simulations using a quasi-two-dimensional model show good agreement with the experimental observations. The frequency of oscillation of the velocity component in the x direction is twice that of the velocity component in y direction. The model was based on the solution of the conservation equations coupled with an immersed boundary method to solve the dynamics of the solid body. It was possible to compute the entire trajectory and velocity of the magnet. It was found that the initial motion is entirely a rectilinear accelerated motion in the x direction (see Fig. 8), after this stage the magnet oscillates periodically, as observed in the experiments. The frequency and amplitude of the oscillation of the magnet show a linear dependence as a function of the Reynolds number. From Fig. 10, it can be observed that the quasi-two-dimensional model predicts very well the Reynolds number based on the velocity of the magnet in the range of low currents in which the vortex street is not present. Once the vortex shedding appears, the model underpredicts the Reynolds number, and then it can be inferred that at higher electric currents three-dimensional effects not taken into account in the quasi-two-dimensional approach become important. Another difference between the numerical results and the experimental observations of the flow pattern that could be attributed to three-dimensional effects is the alignment of the vortices in the wake of the magnet. This difference can be observed when we compare the particle tracking of the computed flow (Fig. 6) with the ink visualizations (Fig. 2).

ACKNOWLEDGMENTS

This research was supported by CONACYT (MX), under projects 258623 and 240785. A.F. thanks the Cátedras program of CONACYT (MX) and S.P. thanks the PRODEP postdoctoral fellowship program of SEP, México.

[1] Y. D. Afanasyev, Wakes behind towed and self-propelled bodies: Asymptotic theory, Phys. Fluids **16**, 3235 (2004).

[2] Y. D. Afanasyev and V. N. Korabel, Wakes, and vortex streets generated by translating force, and force doublet: Laboratory experiments, J. Fluid Mech. **553**, 119 (2006).

[3] J. Román, A. Figueroa, and S. Cuevas, Wake patterns behind a magnetic obstacle in an electrolyte layer, Magnetohydrodynamics **53**(1), 55 (2017).
[4] F. Samsami, Y. Kolesnikov, and A. Thess, Vortex dynamics in the wake of a magnetic obstacle, J. Vis. **17**, 245 (2014).
[5] S. Prinz, V. Bandaru, Y. Kolesnikov, D. Krasnov, and T. Boeck, Numerical simulations of magnetohydrodynamic flows driven by a moving permanent magnet, Phys. Rev. Fluids **1**, 043601 (2016).
[6] S. Cuevas, S. Smolentsev, and M. Abdou, On the flow past a magnetic obstacle, J. Fluid Mech. **553**, 227 (2006).
[7] E. V. Votyakov, Y. Kolesnikov, O. Andreev, E. Zienicke, and A. Thess, Structure of the Wake of a Magnetic Obstacle, Phys. Rev. Lett. **98**, 144504 (2007).
[8] Y. D. Afanasyev and V. N. Korabel, Starting vortex dipoles in a viscous fluid: Asymptotic theory, numerical simulations, and laboratory experiments, Phys. Fluids **16**, 3850 (2004).
[9] Y. D. Afanasyev, Formation of vortex dipoles, Phys. Fluids **18**, 037103 (2006).
[10] A. Figueroa, F. Demiaux, S. Cuevas, and E. Ramos, Electrically driven vortices in a weak dipolar magnetic field in a shallow electrolytic layer, J. Fluid Mech. **641**, 245 (2009).
[11] W. Thielicke and E. J. Stamhuis, PIVlab - Time-Resolved Digital Particle Image Velocimetry Tool for MATLAB, Version 1.41, 2014, doi:10.6084/m9.figshare.1092508.
[12] C. S. Peskin, Numerical analysis of blood flow in the heart, J. Comp. Phys. **25**, 220 (1977).
[13] G. Tryggvason, R. Scardovelli, and S. Zaleski, *Direct Numerical Simulations of Gas-Liquid Multiphase Flows*, 1st ed. (Cambridge University Press, Cambridge, 2011).
[14] S. Piedra, E. Ramos, and J. R. Herrera, Dynamics of two-dimensional bubbles, Phys. Rev. E **91**, 063013 (2015).
[15] Y. Sui, Y. T. Chew, P. Roy, and H. T. Low, A hybrid immersed-boundary, and multi-block lattice Boltzmann method for simulating fluid, and moving-boundaries interactions, Int. J. Numer. Methods Fluids **53**, 1727 (2006).
[16] C. C. Liao, Y. W. Chang, C. A. Lin, and J. M. McDonough, Simulating flows with moving rigid boundary using immersed-boundary method, Comput. Fluids **39**, 152 (2010).
[17] N. Sharma and N. A. Patankar, A fast computation technique for the direct numerical simulation of rigid particulate flows, J. Comp. Phys. **205**, 439 (2005).
[18] A. Ghasemi, A. Pathak, and M. Raessi, Computational simulation of the interactions between moving rigid bodies, and incompressible two-fluid flows, Comput. Fluids **94**, 1 (2014).
[19] Y. Afanasyev and Korabel, Wakes, and vortex streets behind a localized force: Numerical simulations, Commun. Nonlinear Sci. Numer. Simul. **13**, 1101 (2008).
[20] S. Cuevas, S. Smolentsev, and M. Abdou, Vorticity generation in creeping flow past a magnetic obstacle, Phys. Rev. E **74**, 056301 (2006).
[21] C. H. K. Williamson, Vortex dynamics in the cylinder wake, Annu. Rev. Fluid Mech. **28**, 477 (1996).
[22] V. Roig, M. Roudet, F. Risso, and A. M. Billete, Dynamics of a high-Reynolds-number bubble rising within a thin gap, J. Fluid Mech. **707**, 444 (2012).